A Novel Contingency-Aware Primary Frequency Control for Power Grids With High CIG-Penetration

Oleg Olegovich Khamisov, Mazhar Ali, *Graduate Student Member, IEEE*, Timur Sayfutdinov, *Member, IEEE*, Yan Jiang, Vladimir Terzija, and Petr Vorobev

***Abstract*—The ever-growing trend of Converter-Interfaced Generation (CIG) integration in electrical power grids has led to a tremendous concern about systems' inertia, stability, and frequency regulation effectiveness. During contingencies, like the loss of a large generator, the primary frequency control is deployed to compensate for the frequency drop. However, as CIG penetration grows, traditional primary frequency control becomes less effective in mitigating significant post-contingency frequency deviations. To address this problem, we introduce a novel control framework that fully utilizes the proportional primary frequency control concept manifested in the contingency-aware control discontinuity. The proposed framework collects information about the disturbance and redistributes control gains according to the pre-calculated optimal strategy employing dynamic properties of both synchronous generation and CIG. It incorporates a novel frequency security assessment using frequency majorant functions, providing a conservative low boundary estimate of the frequency nadir. Numerical studies demonstrate that this proposed control strategy reduces nadir deviation by 49% and shortens the transient period by 30%. Furthermore, we illustrate the optimization of droop control gains considering CIG characteristics, such as location and inertia, to enhance system stability by allowing CIGs to perform primary frequency control functions from synchronous generators.**

***Index Terms*—Contingency-aware control, converter-interfaced generation, primary frequency control.**

NOMENCLATURE

CCL	Current Control Loop.
CIG	Converter-Interfaced Generator.
COI	Center-of-Inertia.
DAE	Differential-Algebraic Equations.
D.C.	Difference of Convex Functions.
FFC	Fast-Frequency Control.
MPC	Model Predictive Control.
PLL	Phase-Locked Loop.
TSO	Transmission System Operator.
VSC	Voltage Source Converter.

Variables

$\mathbf{p}$	Line power flows.
$\mathbf{p}^e$	Nodal power injections at buses.
$\mathbf{p}^m$	Mechanic power injections at generators.
$\mathbf{p}^{CIG}$	Power outputs of CIGs.
$\mathbf{r}$	Droop coefficients vector.
$\mathbf{x}_a$	Algebraic state variables.
$\mathbf{x}_d$	Differential state variables.
$\boldsymbol{\theta}$	Bus phase angles.
$\boldsymbol{\theta}^m$	Phase angles measurements.
$\boldsymbol{\omega}$	Deviations of bus frequencies.
$\boldsymbol{\omega}^m$	Frequency deviations measurements.
$\boldsymbol{\psi}$	Auxiliary PLL variables.

Sets

$\mathbb{R}$	Set of real numbers.
$\mathbf{N}$	Set of buses.
$\mathbf{N}_1$	Set of synchronous generators.
$\mathbf{N}_2$	Set of load buses.
$\mathbf{N}_3$	Set of CIGs.
$\mathbf{Q}$	Set of lines.
$\mathbf{R}^d$	Set of optimal droop coefficients vectors.
$\mathbf{P}^d$	Set of disturbance vectors.

Parameters

$\mathbf{A}$	State-space matrix.
$\mathbf{B}$	Diagonal matrix of line parameters.
$\mathbf{C}$	Incidence matrix of the graph.
$\mathbf{D}$	Diagonal matrix of generators mechanical damping coefficients and frequency-dependent loads coefficients.
$\mathbf{I}$	Identity matrix.
$\mathbf{K}^i$	Matrix of PLL integral coefficients.
$\mathbf{K}^p$	Matrix of PLL proportional coefficients.
$\mathbf{L}_1$	Diagonal matrix of ones for indexes $\mathbf{N}_1 \cap \mathbf{N}_3$.

Manuscript received 27 April 2023; revised 8 October 2023; accepted 19 November 2023. Date of publication 12 December 2023; date of current version 20 June 2024. This work was supported by the Ministry of Science and Higher Education of Russian Federation through the AMPaC Megagrant Project under Grant 075-10-2021-067, Grant Identification code 000000S707521QJX0002. Sections VI and VII were prepared as a part of UNIFY Project supported by Russian Science Foundation, under Project 22-49-02065. Paper no. TPWRS-00618-2023. *(Corresponding author: Oleg Olegovich Khamisov.)*

Oleg Olegovich Khamisov is with the Center for Energy Science and Technology, Skolkovo Institute of Science and Technology, 121205 Moscow, Russia (e-mail: oleg.khamisov@skoltech.ru).

Mazhar Ali is with the Department of Electrical and Computer Engineering, University of Central Florida, Orlnado, FL 32816 USA (e-mail: mazhar.ali@ucf.edu).

Timur Sayfutdinov is with the School of Advanced Technology, Xi'an Jiaotong-Liverpool University, Suzhou 215000, China (e-mail: tsaifutdinov@gmail.com).

Yan Jiang is with the Department of Electrical and Computer Engineering, University of Washington, Seattle, WA 98195 USA (e-mail: jiangyan@uw.edu).

Vladimir Terzija is with the School of Engineering, Merz Court E4.41, Newcastle University Newcastle, NE1 7RU Newcastle upon Tyne, U.K. (e-mail: vladimir.terzija@ncl.ac.uk).

Petr Vorobev is with Nanyang Technological University, Singapore 639798 (e-mail: petrvorob@gmail.com).

Color versions of one or more figures in this article are available at https://doi.org/10.1109/TPWRS.2023.3339596.

Digital Object Identifier 10.1109/TPWRS.2023.3339596

$\mathbf{L_2}$	Diagonal matrix of ones for indexes $\mathbf{N}_2 \cap \mathbf{N}_3$.
$\mathbf{M}$	Diagonal matrix of matrix generators inertia constants.
$\mathbf{p}^d$	Disturbance vector.
$\mathbf{T}^{CIG}$	Diagonal matrix of current control time constants.
$\mathbf{T}^t$	Diagonal Matrix of turbine time constants.
$\mathbf{T}^v$	Diagonal Matrix of governor time constants.
$t_{\max}$	Time frame for the largest frequency deviation.
$\mathbf{v}$	Governor valves positions.
$\boldsymbol{\rho}$	Vector of all ones.

Functions

$\mathbf{F}(\mathbf{r})$	Frequency security assessment based on exact frequency nadir.
$\boldsymbol{\mathcal{F}a}(:)$	Function denoting a algebraic equations set.
$\boldsymbol{\mathcal{F}d}(:)$	Function denoting a differential equations set.
$\boldsymbol{\mathcal{M}}(t, \mathbf{r})$	Frequency majorant function.
$\mathbf{G}(\mathbf{r})$	Frequency security assessment based on frequency majorant function.

I. INTRODUCTION

THE modern electric power industry is undergoing a massive transition driven by the imperative to address clean energy targets. Over the last decade, most countries have set ambitious goals to reduce their carbon footprints drastically, marking a pivotal shift in the power grid landscape. This paradigm shift is reinforced by the recent developments in power electronics technologies, which have paved the way for the extensive integration of Renewable Energy Sources based on Converter-Interfaced Generators (CIG) [1]. This development has impacted the dynamics of power systems predominantly, reducing overall system inertia and fault levels. It has also negatively impacted the effectiveness of power system balancing services, notably frequency regulation frameworks [2].

The most severe frequency deviations transpire after a critical active power imbalance, typically resulting from a sudden loss of a generator, disconnection of an inter-tie line, or connection/disconnection of large loads. As a result, the system's frequency starts to deviate from its nominal value, either dropping or rising. In response to these deviations, primary frequency control is activated to recover frequency without violating statutory limits [3]. Once the system stabilizes at a new steady state, the secondary frequency control indemnifies frequency to its nominal value [4]. After the primary frequency control response, a new steady-state frequency is achieved, which depends on the magnitude of the active power imbalance and the primary frequency control loop settings of all the generators involved.

Immediately after a contingency event, such as the loss of a large generator, the system's inertia level plays a crucial role in shaping the transient period. During this phase, the system frequency initially drops to its minimum value referred to as the frequency nadir.[1] Subsequently, the frequency starts to recover due to the primary frequency control actions. According to principles of system dynamics, systems with lower inertia have larger frequency nadirs and oscillations of the frequency profile [5]. Fig. 1 illustrates this attribute with a power system of different inertial levels. It is observable that a low-inertia system exhibits a considerably larger frequency nadir compared to a system with standard levels of inertia.

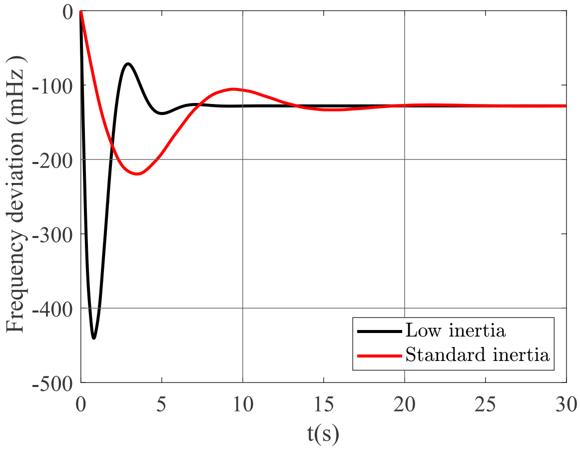

Fig. 1. Frequency profiles of a power system with different inertia levels.

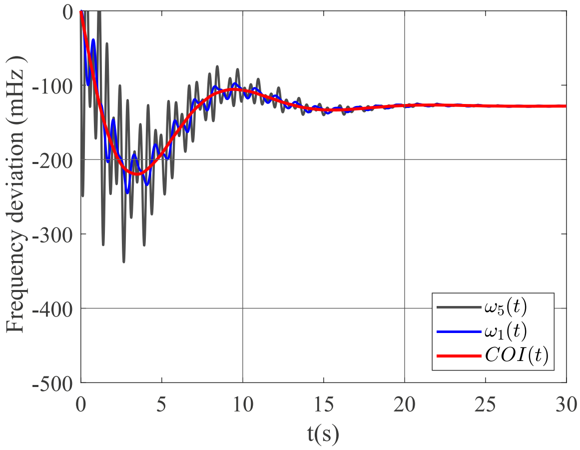

Fig. 2. Frequency deviation for generator 5 (black curve), generator 1 (blue curve), and the Center-of-Inertia (COI) frequency (red curve).

As the modern electric grid will gradually decommission conventional synchronous generators in favor of the high penetration of converter interfaced generation, substantial deviations in frequency nadirs are inevitable. In a multi-machine power system, individual generator frequency drop depends on the electrical proximity to the imbalance location and its inertial nature. Therefore, the dominant frequency deviation location hinges on the imbalance location and the generator's inertial properties.

To illustrate this point, let us consider the dynamics of an IEEE 39-bus network with a power imbalance location at Bus 30, as outlined in [6]. Fig. 2 depicts the spatial characteristics of the system frequency such that the variation between one of the two generator frequencies is easily observable. In this case, generator 5 exhibits large frequency nadir deviations in its frequency profile. This is due to the proximity of generator

---

[1] The most critical dynamic feature of a power system resilience is the frequency nadir, which indicates a minimum post-contingency system frequency.

5 to the region of imbalance caused by the lost generation, in contrast to generator 1.

In determining primary frequency control parameters, the Transmission System Operator (TSO) ensures that system frequency lies within the operational (i.e., ± 0.2 Hz) and statutory (i.e., ± 0.5 Hz) limits [7]. Consequently, dynamic studies are required to confirm that statutory limits for the frequency deviation remain within the bounds for the most severe frequency events, which tend to be system-specific. Any violation could lead to the System Integrity Protection Schemes response, such as under-frequency load-shedding. In some scenarios, the system might infringe on a sequence of cascading events, potentially leading to a system blackout [8]. With the growing penetration of CIGs, the entire system operation has become more challenging. Therefore, there is an urgent need to develop more robust and effective control strategies to minimize frequency deviations from the nominal value.

A review of modern control methods for frequency control can be found in [9] and from the context of large-scale dynamic system control from [10]. An exhaustive literature search reveals the following notable works.

The first set of contributions includes Primal-Dual methods to determine the optimal steady-state of a power grid from a frequency control perspective. These techniques utilize a continuous optimization algorithm, such as gradient descent, to find the optima of the corresponding optimization problem. A two-stage distributed gradient descent/ascent algorithm was introduced, as described in [11], [12], to execute both frequency control and congestion management problems. The interior-point method was proposed in [13], [14] for frequency control in star and tree-topology grids, respectively.

The second category comprises Proportional Integral control-based approaches, where an integral component is introduced to the conventional droop control scheme to improve system dynamics. In addition to the novel control scheme, in [15], [16], control efficiency is mainly increased by utilizing information about frequency deviations from the neighboring buses. In [17], adaptive control gains are proposed to reduce the cost of the control actions.

The quadratic regulator design techniques constitute additional efforts to improve frequency control. These approaches aim to derive solutions by analyzing the transient dynamics of power grids. In [18], [19], [20], Automatic Generation Control is enhanced to operate in low-inertia systems. In these works, authors optimize the integral of frequency deviation norm squared over a time interval from zero to infinity.

The Virtual Inertia concept is also worth mentioning for the CIGs, where power electronics devices emulate the synchronous generator dynamics. For example, in [21], [22] Virtual Inertia concept was applied to fully-rated converter wind turbines, Doubly-fed Induction Generator wind turbines in [23], Photovoltaics in [24], Electric Vehicles in [25], and other Distributed Energy Resources in [26].

To address rapid frequency response in low inertia grids, [27], [28] introduced Model Predictive Control (MPC)-based Fast-Frequency Control (FFC) techniques. In [27], centralized and decentralized MPC-based FFC for low-inertia grids with Voltage Source Converters (VSCs) were introduced. These approaches are activated in response to significant disturbances to ensure that frequency deviation and the Rate of Change of Frequency remain within operator-defined limits. The study enhances frequency prediction using Center-of-Inertia (COI) frequency dynamics from [29] and estimates the parameters of the frequency response model based on historical data. Additionally, it improves computational efficiency for decentralized MPC through offline explicit solution schemes.

In the decentralized MPC [27], each VSC utilizes local measurements and offers spatially proportional support for disturbance mitigation. Consequently, converters located closer to the disturbance provide more support to reduce stress on the transmission lines and minimize losses. Similarly, [28] provides an improved MPC-based FFC method for frequency response with Energy Storage Systems. The MPC identifies Inertial Response time during the primary frequency response for improved parameter estimation. This approach can restore frequency to the initial synchronous state and is robust against parameter changes and communication delays. These MPC techniques act as an auxiliary layer for enhancing primary frequency response in low inertia power systems. However, their implementation comes with challenges such as computational complexity, susceptibility to communication disruptions, and the need for precise modeling and tuning for optimal performance.

Finally, it is also noteworthy to highlight the potential of machine learning and artificial intelligence techniques in various aspects of power system control and management, including primary frequency control [30], [31], [32], [33]. Existing techniques fall short in explicitly modeling power systems with CIGs. These methods integrate a conventional frequency security assessment within an optimization problem to minimize frequency deviations following a disturbance. These assessments rely on COI dynamics or direct nadir assessment using oscillatory frequency trajectories.

However, as converter interfaced generation penetration grows, substantial post-contingency frequency profiles are expected due to the reduced overall system inertia. Thus, the COI-based assessments prove inadequate for accurately capturing post-contingency frequency dynamics. The COI estimates are primarily influenced by the overall system's inertia, overlooking the individual generator frequency oscillations that can significantly impact frequency nadir. It provides a rough estimate of particular bus frequency behavior, focusing on dominant low-frequency modes driven by power imbalances while neglecting smaller participation factor modes contributing to additional oscillations.

Additionally, a direct nadir assessment using oscillatory frequency trajectories poses computational challenges. These include constrained optimization using zero-order methods due to the multiple extrema nature of the frequency contours. It entails the potential identification of local optima and the risk of missing instances of system instability when high-gain proportional controllers are applied over limited time interval.

This work introduces a novel "Piece-wise Proportional and Location-sensitive Primary Frequency Control" (PILOT) framework capable of exploiting information about the grid topology and CIG dynamics. Within this framework, a power system model that includes CIG dynamics is integrated. It introduces a robust frequency security assessment approach using a novel frequency majorant function, which provides a more conservative estimate of the frequency nadir compared to the traditional COI model. This majorant function yields a uni-modal conservative lower boundary for each machine's actual multi-extremum frequency in the power system. Unlike the COI dynamics, it considers all system modes, ensuring a more reliable frequency estimate. Furthermore, the mathematical properties of the majorants also lead to computationally tractable optimization, reducing computational complexity and burden compared to exact direct nadir assessment.

The PILOT framework leverages the "offline optimization/computations and online action-matching" configuration to execute the enhanced primary frequency control. It comprises two main stages: planning and control. Before the real-time operation, the planning stage simulates all possible faults that may occur in the system, and derives a vector of control gains (one per generator) that would ensure the lowest possible nadir in the system's post-contingency dynamics.

The control phase continuously monitors the system's state. During the contingency event, it determines the location of a disturbance based on the data collected. Subsequently, for a specific disturbance location, it dynamically adjusts the pre-computed droop gains for generators and CIG in real-time to ensure optimal primary frequency response to a given contingency. This data-driven control approach offers a significant reduction of frequency deviation utilizing fast converter response despite the complicated dynamics of the power grids with high CIG penetration.

The PILOT framework operates in a centralized way. However, centralized communications are required only during the planning stage and monitoring step of the online stage. After the disturbance location is identified, the control operates in a decentralized way similar to a standard proportional control. As a result, PILOT explicitly minimizes frequency deviations, without requiring large amounts of data to be exchanged in on-line stage. In comparison, aforementioned distributed control approaches [11], [12], [13], [14] utilize continuous versions of different optimization methods, which allow convergence to a desired steady state, but do not guarantee safe transient performance.

The theoretical results for the PILOT framework are validated with case studies employing detailed sub-transient reactance generator and multistage-turbine models from Power System Toolbox [6], along with explicit models of interfacing converters as presented in [34]. An IEEE 39-bus network served as a benchmark to illustrate the effectiveness of the proposed framework. The results highlight that the proposed PILOT framework leads to a 49% reduction in frequency nadir deviation and a 30% reduction in the transient period. Additionally, studies demonstrate that low inertia power grids can substantially improve system stability when optimizing the droop control gains based on the characteristics of each CIG, including their location and dynamics. The key contributions within the proposed PILOT framework are as follows,

1) A contingency-aware piece-wise proportional primary frequency control that dynamically adjusts droop control gains for an optimized response to specific disturbances.
2) An improved frequency security assessment based on the novel frequency majorant function, a uni-modal conservative estimate of each machine's actual multi-extremum frequency by accounting for all the system modes.
3) A computationally tractable optimization formulation to calculate optimal proportional control gains for a given disturbance, incorporating characteristics of both traditional generation and CIG.
4) Demonstrated the potential of CIGs to assume control of primary frequency response from the traditional synchronous generators, resulting in improved grid stability.

The paper structure is as follows: Section II presents a mathematical model describing power grid frequency dynamics and the associated challenges in nadir minimization. Section III presents two algorithms outlining the planning and operation stages of the proposed control algorithm. Section IV provides the linearized dynamical model of the system for use in the planning stage. Section V covers the derivation of the computationally tractable nadir assessment. Section VI describes the optimization procedure for the planning stage of the controller. Section VII includes numerical validation of the proposed algorithmic framework and a comparison to virtual inertia approach for a nonlinear detailed power system model. Finally, conclusions are provided in Section VIII.

II. MATHEMATICAL MODELING AND PRELIMINARIES

Let us consider a multi-machine electrical power system as a directed connected graph $\mathbf{\Gamma} = (\mathbf{N}, \mathbf{Q})$. Here, $\mathbf{N} = \{1, \ldots, n\}$ represent a set of "n" buses (vertices) and $\mathbf{Q}$ denotes the set of "q" lines (edges). The set $\mathbf{N}$ consists of two disjoint sets: a set of "n_1" synchronous generators denoted by $\mathbf{N}_1 \subseteq \mathbf{N}$, and a set of "$n_2$" loads described by $\mathbf{N}_2 \subseteq \mathbf{N}$. In addition, some of the buses (both loads and synchronous generators) can have Converter-Interfaced (CI) generators. We denote the corresponding set as $\mathbf{N}_3 \subseteq \mathbf{N}$ with "n_3" elements. The general dynamics of the power grid can be represented by a Differential-Algebraic Equations (DAE) model with m_d-differential and m_a-algebraic equations:

$$\dot{\mathbf{x}}_d = \boldsymbol{\mathcal{F}_d}\left(\mathbf{x}_d, \mathbf{x}_a, \mathbf{r}, \mathbf{p}^d\right), \tag{1a}$$

$$\mathbf{0} = \boldsymbol{\mathcal{F}_a}\left(\mathbf{x}_d, \mathbf{x}_a, \mathbf{r}, \mathbf{p}^d\right). \tag{1b}$$

Here, $\boldsymbol{\mathcal{F}_d} : \mathbb{R}^{(m_d+m_a+n+n_1+n_3)} \rightarrow \mathbb{R}^{m_d}$ denotes the m_d-number of differential equations representing dynamics of the synchronous machines and CIGs. While $\boldsymbol{\mathcal{F}_a} : \mathbb{R}^{(m_d+m_a+n+n_1+n_3)} \rightarrow \mathbb{R}^{m_a}$ constitutes nonlinear algebraic equations which are mainly load flow equations. Both $\boldsymbol{\mathcal{F}_d}$ and $\boldsymbol{\mathcal{F}_a}$ represent a smooth map, i.e., continuously differentiable.

In (1), vector $\mathbf{x}_d \in \mathbb{R}^{m_d}$ represents dynamic state variables like bus frequency deviations, generators' rotor angles and angular velocities. While, vector $\mathbf{x}_a \in \mathbb{R}^{m_a}$ refers to algebraic state variables vector namely voltage magnitudes and phase angles.

Finally, $\mathbf{r} \in \mathbb{R}^{n_1+n_3}$ represent a vector of droop coefficients and $\mathbf{p}^d \in \mathbb{R}^{n_1+n_2}$ is a disturbance vector.

Within this setup, vector of frequency deviations $\boldsymbol{\omega}$ is a subvector of $(\mathbf{x}_d^\top, \mathbf{x}_a^\top)^\top$. Therefore, frequency nadir as a function of droop coefficients can be defined as,

$$\mathbf{F}(\mathbf{r}) = \max_{i \in \mathbf{N}} \max_{t \in [0, t_{\max}]} |\boldsymbol{\omega}_i(t, \mathbf{r})|. \tag{2}$$

In (2), $t_{\max}$ defines the length of the time horizon during which the largest frequency deviation transpires. This time horizon can vary from seconds to minutes depending upon various factors, most notably the overall damping characteristics of the system and the given contingency nature [35], [36]. Ideally, one would like to minimize the frequency nadir after a disturbance as,

$$\min_{\mathbf{r} \in \mathbb{R}^{n_1+n_3}} \mathbf{F}(\mathbf{r}), \tag{3}$$

However, such direct optimization is challenging because:

1) Trajectories $\boldsymbol{\omega}_i(t, \mathbf{r})$ are defined by a nonlinear DAE model (1). Thus, an analytic solution is usually not available. The objective function in (3) can only be treated as a non-differential (due to maximization over i) black box function, and optimization is limited to a zero-order approach. Due to the oscillatory nature of the frequency, this function has multiple extrema, and zero-order methods efficiency is severely limited.
2) In numerical simulations, the inner maximum over t can be considered only over a limited interval. It is generally known that high-gain proportional controllers can cause system instability, which may go undetected during such a short observation time.
3) The numerical solution of (1) is a computationally expansive task. Therefore, the optimization procedure and calculating inner maxima are numerically expensive.

The direct nadir optimization problem (3) yields a number of both analytical and numerical challenges. The methodology to overcome the latter is given in the following section.

III. Piece-Wise Proportional and Location Sensitive Primary Frequency Control Algorithm

A novel nadir optimization approach for primary frequency control is presented in this section to overcome the computational challenges associated with direct optimization (3). The proposed framework is referred to as the "Piece-wise Proportional and Location-sensitive Primary Frequency Control" (PILOT) framework. The PILOT algorithmic structure comprises two algorithms. The Algorithm 1 is an offline action focused on calculating the optimal primary frequency system response for each contingency from a predefined set $\mathbf{P}^d = \{\mathbf{p}^{d1}, \mathbf{p}^{d2}, \ldots, \mathbf{p}^{d\max}\}$. The online Algorithm 2 monitors the system state in real-time and delineates control gains according to the pre-calculated primary response strategy. The set $\mathbf{P}^d$ consists of contingencies that Algorithm 2 identifies during online operation. The algorithms themselves do not impose any limitations on the set P^D. However, the disturbance type must be recognizable in real time during the operation of Algorithm 2.

```
Algorithm 1: Optimization of Control Parameters.
Input: Functions $\mathcal{F}_d$ and $\mathcal{F}_a$, set $\mathbf{P}^d$ of disturbance
  vectors $\mathbf{p}^d$ (one for each credible contingency).
Output: Mapping $\boldsymbol{\Omega} : \mathbf{P}^d \leftrightarrow \mathbf{R}^d$ between disturbances
  and vectors of control coefficients for optimal response.
Algorithm steps:
Step 1: For each $\mathbf{p}^d \in \mathbf{P}^d$ perform steps 2 to 6; Exit;
Step 2: Calculate state matrix $\mathbf{A}(\mathbf{r})$ by linearizing
  system (1).
Step 3: Derive a function estimating the maximal
  frequency deviation $\mathbf{G} : \mathbb{R}^n \to \mathbb{R}$ such that
      $\mathbf{G}(\mathbf{r}) \geq \mathbf{F}(\mathbf{r})$;
Step 4: Solve
      $\min_{\mathbf{r} \in \mathbb{R}^{n_1+n_3}} \mathbf{G}(\mathbf{r}),$    (4a)
      $\max \{\Re(\mathrm{eig}(\mathbf{A}(\mathbf{r})))\} \leq -\epsilon;$    (4b)
Step 5: Verify that the obtained solution $\mathbf{r}^*$ using the full,
  nonlinear DAE model (1);
Step 6: Define map, $\boldsymbol{\Omega}(\mathbf{p}^d) \triangleq \mathbf{r}^*$;
```

One approach involves using vectors corresponding to significant credible contingencies at each bus. Additionally, as shown in [37], the integral of the disturbance vector can be determined using only frequency and electrical power integral measurements. Moreover, if the grid has extensive metering equipment like phase measurement units, disturbances can be identified with high precision, as depicted in [38]. A summary of both algorithms is provided here, followed by a detailed discussion of the algorithmic steps in the subsequent sections.

All steps outlined in the Algorithm 1 aim to overcome computational challenges associated with direct optimization (3). Step 1 initiates with a disturbance vector $\mathbf{p}^d$ from the set of disturbances $\mathbf{P}^d$. It executes steps 2 to 6 to calculate the corresponding optimal droop coefficients vector $\mathbf{r}^*$. In step 2 of the Algorithm 1, a linearized system matrix $\mathbf{A}(\mathbf{r})$ is derived to reduce the computational complexity for subsequent steps. In step 3, the formulation of the assessment function "$\mathbf{G}(\mathbf{r})$" leads to a considerable reduction in computational complexity and computation burden. The function $\mathbf{G}(\mathbf{r})$ is based on the novel frequency majorant function, which provides a conservative low boundary estimate of the frequency nadir of each machine. It is important to note that no technique guarantees escape from the local minima of a black box function. Therefore, reducing the number of local minima is pivotal for achieving good optimization results. Subsequently, it will be demonstrated that the function $\mathbf{G}(\mathbf{r})$ exhibits fewer local optima than the objective function in (3).

In step 4, we employ a zero-order optimization method to solve (4a) with eigenvalues constraint (4b). Since the matrix $\mathbf{A}(\mathbf{r})$ is a linearization and can provide an approximation of the real system dynamics due to parameter variations, a threshold denoted as "ϵ" was introduced to serve as a stability margin for the algorithmic process.

Algorithm 2: Frequency Control.

```
Input: Disturbance vector $\mathbf{p}^d$, default control vector $\mathbf{r}^0$.
Output: Control vector $\mathbf{r}$.
Algorithm steps:
Step 1: If $\mathbf{p}^d \notin \mathbf{P}^d$ set $\mathbf{r}$ to default value $\mathbf{r}^0$; Exit;
Step 2: Set $\mathbf{r} = \mathbf{\Omega}(\mathbf{p}^d)$; Exit;
```

Finally, step 5 utilizes a detailed dynamical model of a multi-machine power grid to validate the optimization results. To conclude, Algorithm 1 serves the purpose of creating a mapping, referred to as $\mathbf{\Omega}$, between credible contingencies $\mathbf{p}^d \in \mathbf{P}^d$ and control vectors $\mathbf{r} \in \mathbf{R}^d$. Here, $\mathbf{P}^d$ and $\mathbf{R}^d$ refer to the sets of credible contingencies and control coefficient vectors, respectively. Once this mapping is established, it facilitates the real-time implementation of a new piece-wise proportional primary frequency control strategy. Algorithm 2 is specifically tailored for driving this control objective. In this context, the algorithm already has access to pre-computed optimal droop control values. Thus, whenever the system encounters a credible contingency originating from $\mathbf{P}^d$, it readily substitutes the corresponding optimal control vector from $\mathbf{R}^d$ within the droop control system.

The two stage approach, utilized above is aimed to minimize computational complexity of real-time operation of Algorithm 2, while performing detailed optimization in Algorithm 1. Both algorithms require centralized implementation, However, online stage exchanges information only during step 1, when vector of control gains is chosen. Further operation is completely decentralized. In the following sections, we describe all the critical steps of Algorithm 1 in more detail.

IV. SYSTEM LINEARIZATION AND MATRIX $\mathbf{A}(\mathbf{r})$

A classical generator model [4] is used for the linearized system "$\mathbf{A}(\mathbf{r})$" at step 2 of Algorithm. 1. This model assumes synchronous generators with turbines and governors. Given that frequency variations remain minimal compared to the nominal frequency, even in the aftermath of significant contingencies, linearizing the DAE model (1) around an equilibrium point is justified. During power imbalance scenarios, voltage changes are typically minimal. Hence, we assume that the voltage magnitudes at all buses are 1 per unit (p.u.). The CIGs are represented as linear Phase-Locked Loop (PLL) and first-order Current Control Loop (CCL) converters.

Under these assumptions, the following model describes the frequency dynamics of the multi-machine power system as,

$$\dot{\boldsymbol{\theta}} = \boldsymbol{\omega} \tag{5a}$$

$$\mathbf{M}\dot{\boldsymbol{\omega}}_{\mathbf{N}_1} = -\mathbf{D}_{\mathbf{N}_1}\boldsymbol{\omega}_{\mathbf{N}_1} - \mathbf{p}^e_{\mathbf{N}_1} + \mathbf{p}^m + \mathbf{p}^d_{\mathbf{N}_1} + \mathbf{L}_1\mathbf{p}^{CIG}_{\mathbf{N}_1\cap\mathbf{N}_3} \tag{5b}$$

$$\mathbf{T}^t\dot{\mathbf{p}}^m = -\mathbf{p}^m + \mathbf{v} \tag{5c}$$

$$\mathbf{T}^v\dot{\mathbf{v}} = -\mathbf{v} - \mathrm{diag}(\mathbf{r}_1, \ldots, \mathbf{r}_{n_1})\boldsymbol{\omega}_{\mathbf{N}_1} \tag{5d}$$

$$\mathbf{0} = -\mathbf{D}_{\mathbf{N}_2}\boldsymbol{\omega}_{\mathbf{N}_2} - \mathbf{p}^e_{\mathbf{N}_2} + \mathbf{p}^d_{\mathbf{N}_2} + \mathbf{L}_2\mathbf{p}^{CIG}_{\mathbf{N}_1\cap\mathbf{N}_3} \tag{6a}$$

$$\mathbf{0} = \mathbf{B}\mathbf{C}^T\boldsymbol{\theta} - \mathbf{p}, \tag{6b}$$

$$\mathbf{0} = \mathbf{C}\mathbf{p} - \mathbf{p}^e \tag{6c}$$

$$\dot{\boldsymbol{\psi}} = \boldsymbol{\omega}_{\mathbf{N}_3} - \boldsymbol{\omega}^m \tag{7a}$$

$$\boldsymbol{\omega}^m = \mathbf{K}^i\boldsymbol{\psi} + \mathbf{K}^p(\boldsymbol{\omega}_{\mathbf{N}_3} - \boldsymbol{\omega}^m) \tag{7b}$$

$$\boldsymbol{T}^{CIG}\dot{\mathbf{p}}^{CIG} = -\mathbf{p}^{CIG} - \mathrm{diag}(\mathbf{r}_{n_1+1}, \ldots, \mathbf{r}_{n_1+n_3})\boldsymbol{\omega}^m \tag{7c}$$

Here, sets in lower indices are used to denote corresponding sub-vectors and row sub-matrices. All the state variables, including $\mathbf{p}$ and $\mathbf{p}^e$, represent the deviations of the corresponding quantity from its steady-state value. In the DAE model (5)–(7), (5) consist of a classical generator model described by (5a) and (5b), as well as second-order turbine and governor models given by (5c) and (5d). The system (6) consists of algebraic equations. Equation (6a) characterizes frequency-dependent loads, while (6b) and (6c) represent linearization of Kirchhoff's laws. Inverter dynamics are defined by (7). Specifically, (7a) and (7b) pertain to the PLL, while (7c) outlines the CCL.

Details about variables in the system (5)-(7) are as follow: $\boldsymbol{\theta}(t) \in \mathbb{R}^n$ — bus phase angles; $\boldsymbol{\omega}(t) \in \mathbb{R}^n$ — deviations of bus frequencies from the nominal value; $\mathbf{p}^m(t) \in \mathbb{R}^{n_1}$ — mechanic power injections at generators (on top of the steady state power); $\mathbf{p}^e(t) \in \mathbb{R}^n$ — electrical powers at buses; $\mathbf{p}(t) \in \mathbb{R}^q$ — line power flows; $\mathbf{v}(t) \in \mathbb{R}^{n_1}$ — governor valves positions; $\boldsymbol{\theta}^m(t) \in \mathbb{R}^{n_3}$ — phase angles measurements obtained by PLL; $\boldsymbol{\omega}^m(t) \in \mathbb{R}^{n_3}$ — frequency deviations measurements; $\boldsymbol{\psi}(t) \in \mathbb{R}^{n_3}$ — auxiliary PLL variables; $\mathbf{p}^{CIG}(t) \in \mathbb{R}^{n_3}$ — CIG power output.

Parameters of the system have the following meanings: $\mathbf{L_1}$ and $\mathbf{L_2}$ are diagonal matrices with ones in indexes that belong to $\mathbf{N}_1 \cap \mathbf{N}_3$ and $\mathbf{N}_2 \cap \mathbf{N}_3$ respectively and zeros on other places; $\mathbf{M} = \mathrm{diag}(\mathbf{M}_1, \ldots, \mathbf{M}_{n_1}) \succ 0$ is matrix of generators inertia constants; $\mathbf{D} = \mathrm{diag}(\mathbf{D}_1, \ldots, \mathbf{D}_n) \succ 0$ are the mechanical damping coefficients of generators and coefficients for frequency dependent loads; $\mathbf{T}^t = \mathrm{diag}(\mathbf{T}^t_1, \ldots, \mathbf{T}^t_{n_1})$ and $\mathbf{T}^v = \mathrm{diag}(\mathbf{T}^v_1, \ldots, \mathbf{T}^v_{n_1})$ are turbine and governor time constants respectively. $\mathbf{K}^p, \mathbf{K}^i \in \mathbb{R}^{n_3 \times n_3}$ are PLL proportional and integral coefficients; $\mathbf{B} = \mathrm{diag}(\mathbf{B}_1, \ldots, \mathbf{B}_q) \succ 0$ are line parameters that depend on line admittance and steady-state angle differences [39]; $\mathbf{C}$ is the incidence matrix of the graph; $\mathbf{T}^{CIG} = \mathrm{diag}(\mathbf{T}^{CIG}_1, \ldots, \mathbf{T}^{CIG}_{n_3})$ is diagonal matrix of current control time constants. $\mathbf{p}^d \in \mathbb{R}^n$ is a vector of power disturbances at the network buses.

The system described by (5)-(7) constitutes a set of DAE with non-singular submatrix of the algebraic connections. Therefore, it is possible to transform this system into one composed entirely of differential equations. This transformation involves excluding load buses using Kron reduction [40], and for the remaining algebraic equations, simple exclusion of variables $\mathbf{p}$ and $\mathbf{p}^e$ can be applied. Finally, we can write the system (5)-(7) in the following compact form:

$$\dot{\mathbf{x}} = \mathbf{A}(\mathbf{r})\mathbf{x} + \mathbf{P}^d. \tag{8}$$

Here, $\mathbf{x} \in \mathbb{R}^m$ is the vector of states, $\mathbf{A} \in \mathbb{R}^{m\times m}$ is the state matrix, the vector $\mathbf{r} \in \mathbb{R}^{n_1+n_3}$ denotes the set of system parameters (inertia, turbine, and governors time constants, droop coefficients, etc.), and $\mathbf{P}^d \in \mathbb{R}^m$ is the vector that contains p^d after Kron reduction.

A standard approach for frequency security assessment of the system (5)-(7) considers dynamics of its COI, which is defined as follows:

$$\mathrm{COI}(t) = \sum_{i\in\mathbf{N}} \frac{\mathbf{M}_i \boldsymbol{\omega}_i(t)}{\mathbf{M}_i} \tag{9}$$

The dynamics of $\mathrm{COI}(t)$ in a system with varying levels of inertia is presented in Fig. 1. The $\mathrm{COI}(t)$ dynamics depend upon the overall values of the systems' inertia. It can not account for the frequency oscillations of every individual generator, which may drastically affect the frequency nadir value, as shown in Fig. 2. The example from Fig. 2 highlights $\mathrm{COI}(t)$ dynamics for a 10-machine IEEE 39-bus system (red curve) along with frequency dynamics of two other machines (i.e., black and blue curves). It is observable that the $\mathrm{COI}(t)$ dynamics gives only an approximate picture of what happens with frequency on the individual buses, where it indicates additional oscillations with multiple minima and maxima.

The $\mathrm{COI}(t)$ dynamics are determined by the dominant systems' modes (8), which are low-frequency modes primarily excited by the power imbalance disturbance. In contrast, the modes with smaller participation factors may affect additional frequency oscillations at every machine. To achieve a more accurate frequency assessment requires consideration of all system modes and not just the dominant ones.

A novel frequency majorant is presented in the next section to address the limitations of the traditional frequency security assessment.

V. MAXIMAL FREQUENCY DEVIATION ASSESSMENT $\mathbf{G}(\mathbf{r})$

The frequency majorant will provide a uni-modal conservative lower boundary for the actual multi-extremum frequency of every machine in the power system. The majorant incorporates all the system modes, unlike $\mathrm{COI}(t)$, thus providing a more reliable frequency estimation. This majorant can be used in other applications, including minimizing power systems' frequency variations following disturbances.

To derive the frequency majorant, let us start from the solution of the system (8). For an initial condition $\mathbf{x}(0) = \mathbf{0}$, the solution can be written as,

$$\mathbf{x}(t,\mathbf{r}) = (e^{\mathbf{A}(\mathbf{r})t} - \mathbf{I})\mathbf{A}^{+}(\mathbf{r})\mathbf{P}^d. \tag{10}$$

Here, $\mathbf{I}$ is an identity matrix and $\mathbf{A}^{+}(\mathbf{r})$ is a Moore-Penrose pseudoinverse of the state matrix $\mathbf{A}(\mathbf{r})$. Next, the eigenvalue decomposition of the state matrix $\mathbf{A}$ is introduced as,

$$\mathbf{A}(\mathbf{r}) = \mathbf{S}(\mathbf{r})\boldsymbol{\Lambda}(\mathbf{r})\mathbf{S}(\mathbf{r})^{-1}.$$

Here $\boldsymbol{\Lambda}(\mathbf{r}) = \mathrm{diag}(\boldsymbol{\lambda}_1(\mathbf{r}), \ldots, \boldsymbol{\lambda}_n(\mathbf{r}))$ comprises of eigenvalues of $\mathbf{A}$ and $\mathbf{S}(\mathbf{r})$ is the matrix of eigenvectors of $\mathbf{A}$. Let us now denote,

$$\mathbf{H}(\mathbf{r}) = \mathbf{S}(\mathbf{r})\boldsymbol{\Lambda}^{+}(\mathbf{r})\,\mathrm{diag}(\mathbf{S}^{-1}(\mathbf{r})\mathbf{P}^d).$$

Matrix $\mathbf{H}(\mathbf{r})$ has entries $\mathbf{h}_{ij}(\mathbf{r})$. Then, the solution (10) can then be written as follows,

$$\begin{aligned}\mathbf{x}(t,\mathbf{r}) &= (e^{\boldsymbol{\Lambda}(\mathbf{r})t} - \mathbf{I})\mathbf{H}(\mathbf{r})\boldsymbol{\rho}\\ &= (\mathbf{S}(\mathbf{r})e^{\boldsymbol{\Lambda}(\mathbf{r})t}\boldsymbol{\Lambda}^{+}(\mathbf{r})\,\mathrm{diag}(\mathbf{S}^{-1}(\mathbf{r})\mathbf{P}^d) - \mathbf{H}(\mathbf{r}))\boldsymbol{\rho}\\ &= \mathbf{H}(\mathbf{r})(e^{\boldsymbol{\Lambda}(\mathbf{r})t} - \mathbf{I})\boldsymbol{\rho}.\end{aligned} \tag{11}$$

In (11), $\boldsymbol{\rho}$ is vector of ones. We will now derive the frequency majorant function as the minimum (in terms of the absolute value of frequency deviation) of two other functions, namely $\boldsymbol{\mathcal{M}}_i^1(t,\mathbf{r})$ and $\boldsymbol{\mathcal{M}}_i^2(t,\mathbf{r})$ with $i \in \mathbf{N}$. Both functions $\boldsymbol{\mathcal{M}}_i^1(t,\mathbf{r})$ and $\boldsymbol{\mathcal{M}}_i^2(t,\mathbf{r})$ provide an estimation of the lower boundary of the frequency. However, a combination of both functions reduces the estimation conservativeness.

The first function $\boldsymbol{\mathcal{M}}_i^1(t,\mathbf{r})$ is derived as a combination of nonlinear tangents for each mode and gives an approximation for smaller values over t. The second function $\boldsymbol{\mathcal{M}}_i^2(t,\mathbf{r})$ is formulated based on exponential dynamics of the system (8) and gives a good approximation for bigger values over t.

Fig. 3 depicts an explicit comparison among the COI dynamics, frequency deviations, and majorants for generator 1 of a 10-machine and a 48-machine system, respectively. It is observable that either of the majorants or their combination provides a better estimate for the frequency nadir.

To construct the majorant functions, the solution of the system (8) is represented as a sum of trigonometric functions multiplied by exponents. It allows us to employ derivatives and trigonometric functions constraints to formulate tangent-like majornat. The following notations are used for simplicity,

$$\Re\left(\boldsymbol{\Lambda}(\mathbf{r})\right) = \boldsymbol{\Lambda}^r(\mathbf{r}), \quad \Im\left(\boldsymbol{\Lambda}(\mathbf{r})\right) = \boldsymbol{\Lambda}^i(\mathbf{r}).$$
$$\Re\left(\mathbf{H}(\mathbf{r})\right) = \mathbf{H}^r(\mathbf{r}), \quad \Im\left(\mathbf{H}(\mathbf{r})\right) = \mathbf{H}^i(\mathbf{r}).$$

The first majorant $\boldsymbol{\mathcal{M}}_i^1$, is defined as follows,

$$\begin{aligned}\boldsymbol{\mathcal{M}}_i^1(t,\mathbf{r}) = \sum_{j=1}^{m} &|\mathbf{h}_{ij}^i(\mathbf{r})| e^{\boldsymbol{\lambda}_j^r(\mathbf{r})t} \mathbf{min}\{|\boldsymbol{\lambda}_j^i(\mathbf{r})|t, 1\}\\ &+ \sum_{j=1}^{m} |\mathbf{h}_{ij}^r(\mathbf{r})| \mathbf{min}\left\{\boldsymbol{\mathcal{F}}_j^1(\mathbf{r}), \boldsymbol{\mathcal{F}}_j^2(\mathbf{r})t\right\},\end{aligned} \tag{12}$$

where,

$$\begin{aligned}&\boldsymbol{f}_j(t,\mathbf{r}) = e^{\boldsymbol{\lambda}_j^r(\mathbf{r})t}\cos(\boldsymbol{\lambda}_j^i(\mathbf{r})t) - 1,\\ &\boldsymbol{\mathcal{F}}_j^1(\mathbf{r}) = \sup_{\tau>0} |\boldsymbol{f}_j(\tau,\mathbf{r})|, \quad \boldsymbol{\mathcal{F}}_j^2(\mathbf{r}) = \sup_{\tau\geq 0} \left|\boldsymbol{f}_j'(\tau,\mathbf{r})\right|.\end{aligned} \tag{13}$$

Here, the right-hand side of the formula (12) is separated into two sums. The first one is used to approximate the product of exponents and sine functions of each mode. The second one is used to match the product of exponents and cosines. Both approximations are composed of piecewise linear functions to limit the impact of each mode on the overall estimation. Furthermore, it reduces the estimation conservativeness. The second majorant, $\boldsymbol{\mathcal{M}}_i^2$ is defined as follows,

$$\boldsymbol{\mathcal{M}}^2(t,\mathbf{r}) = |\mathbf{H}(\mathbf{r})| e^{\boldsymbol{\Lambda}^r(\mathbf{r})t} + |\boldsymbol{\omega}^*|.$$

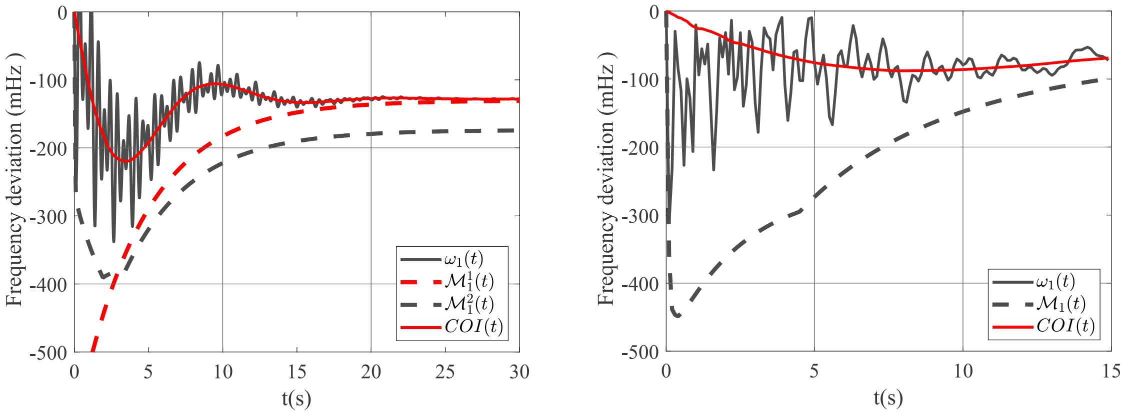

(a) (b)

Fig. 3. COI dynamics, frequency deviation, and majorants for the generator 1 of the (a) 10-machine systen and (b) 48-machine systems (Linearized dynamics).

The following theorem present the key point of this manuscript:

Theorem V.1: For the frequency deviation $\boldsymbol{\omega}_i(t)$, $i \in \mathbf{N}$ the following inequality holds:

$$|\boldsymbol{\omega}_i(t)| \le \boldsymbol{\mathcal{M}}_i(t,\mathbf{r}) = \mathbf{min}\{\boldsymbol{\mathcal{M}}_i^1(t,\mathbf{r}), \boldsymbol{\mathcal{M}}_i^2(t,\mathbf{r})\}.$$

Proof: Inequality $|\boldsymbol{\omega}_i(t)| \le \boldsymbol{\mathcal{M}}_i^2(t,\mathbf{r})$, $i \in \mathbf{N}$ is a direct corollary of the solution form (11). To show that $|\boldsymbol{\omega}(t)_i| \le \boldsymbol{\mathcal{M}}_i^1(t,\mathbf{r})$, $i \in \mathbf{N}$ the following notation $\mathbf{x}(t) = \mathbf{x}^{\sin}(t) + \mathbf{x}^{\cos}(t)$ is used. Here, $\mathbf{x}^{\sin}(t)$ and $\mathbf{x}^{\cos}(t)$ are defined as,

$$\mathbf{x}^{\sin}(t) = \mathbf{H}^i(\mathbf{r})e^{\boldsymbol{\Lambda}^r(\mathbf{r})t}\sin\left(\boldsymbol{\Lambda}^i(\mathbf{r})t\right)\boldsymbol{\rho},$$

$$\mathbf{x}^{\cos}(t) = \mathbf{H}^r(\mathbf{r})(e^{\boldsymbol{\Lambda}^r(\mathbf{r})t}\cos\left(\boldsymbol{\Lambda}^i(\mathbf{r})t\right) - \mathbf{I})\boldsymbol{\rho}.$$

Each of this functions is approximated separately. For $\mathbf{x}_i^{\sin}(t)$ the approximation is given as,

$$|\mathbf{x}_i^{\sin}(t)| = \left|\sum_{j=1}^{m}\mathbf{h}_{ij}^i(\mathbf{r})e^{\boldsymbol{\lambda}_j^r(\mathbf{r})t}\sin\left(\boldsymbol{\lambda}_j^i(\mathbf{r})t\right)\right| \le \sum_{j=1}^{m}|\mathbf{h}_{ij}^i(\mathbf{r})|e^{\boldsymbol{\lambda}_j^r(\mathbf{r})t}\mathbf{min}\{|\boldsymbol{\lambda}_j^i(\mathbf{r})t|, 1\}. \quad (14)$$

For $\mathbf{x}_i^{\cos}(t)$ the approximation is described as,

$$|\mathbf{x}_i^{\cos}(t)| = \left|\sum_{j=1}^{m}\mathbf{h}_{ij}^r f_j(t,\mathbf{r})\right|.$$

Thus, the estimation is given by,

$$|\mathbf{x}_i^{\cos}(t)| \le \sum_{j=1}^{m}|\mathbf{h}_{ij}^r(\mathbf{r})\mathbf{f}_j(t,\mathbf{r})| \le \sum_{j=1}^{m}|h_{ij}^r(\mathbf{r})|\mathbf{min}\left\{\boldsymbol{\mathcal{F}}_j^1(\mathbf{r}), \boldsymbol{\mathcal{F}}_j^2(\mathbf{r})t\right\}. \quad (15)$$

Sum of right hand sides of inequalities (14) and (15) gives $\boldsymbol{\mathcal{M}}^1(t,\mathbf{r})$ from (12). Therefore, $|\mathbf{x}_i(t)| \le \boldsymbol{\mathcal{M}}_i^1(t,\mathbf{r})$ with $i \in \{1,\dots,m\}$ and the theorem is proven. ■

The current stage majorants contain $2\,m$ supremums $\boldsymbol{\mathcal{F}}_j^1(\mathbf{r})$ and $\boldsymbol{\mathcal{F}}_j^2(\mathbf{r})$, which have to be calculated explicitly in order to use (12). For this, let us find moments of time t_j^* and t_j^{**} such that $\boldsymbol{\mathcal{F}}_i^1(\mathbf{r}) = |\boldsymbol{f}_j(t_j^*,\mathbf{r})|$, $\boldsymbol{\lambda}_j^2(\mathbf{r}) = |\boldsymbol{f}_j'(t_j^{**},\mathbf{r})|$. Since cosine is a symmetric function, without loss of generality it can be assumed that $\boldsymbol{\lambda}_j^i(\mathbf{r}) \ge 0$. Note that $\boldsymbol{f}_j(t,\mathbf{r}) \in [0; -2]$. Therefore, the following condition holds,

$$\sup_{\tau \ge 0}|\boldsymbol{f}_j(t,\mathbf{r})| = -\inf_{\tau \ge 0}\boldsymbol{f}_j(t,\mathbf{r}). \quad (16)$$

Let us now find stationary points of $\boldsymbol{f}(t,\mathbf{r})$, i.e. the points where $\boldsymbol{f}'(t,\mathbf{r}) = 0$. In the case when $\boldsymbol{\lambda}_j^r(\mathbf{r})$ and $\boldsymbol{\lambda}_j^i(\mathbf{r})$ are nonzero, the stationary points are given by,

$$t_k = \frac{1}{\boldsymbol{\lambda}_j^i(\mathbf{r})}\left(\arctan\frac{\boldsymbol{\lambda}_j^r(\mathbf{r})}{\boldsymbol{\lambda}_j^i(\mathbf{r})} + \pi k\right),\ k \in \mathbb{N}.$$

From (16) it can be seen, that t_k can be a global maximum only if $\cos(\boldsymbol{\lambda}_j^i(\mathbf{r})t_k) < 0$, therefore only odd values of k are considered. These values of t_k are spaced by 2π, hence all corresponding values of the cosine function are the same (denoted as γ) and $\boldsymbol{f}(t_k,\mathbf{r}) = \gamma e^{\boldsymbol{\lambda}_i^r(\mathbf{r})t_k} - 1$. Since the exponent is a monotonically decreasing function, the first odd stationary point t_2 is the global maximum. With the addition of the cases with $\boldsymbol{\lambda}_j^r(\mathbf{r}) = 0$ and $\boldsymbol{\lambda}_j^i(\mathbf{r}) = 0$, the supremum (13) is reached when,

$$t_j^* = \begin{cases} +\infty, & \text{if } \boldsymbol{\lambda}_j^i(\mathbf{r}) = 0, \\ \frac{\pi}{\boldsymbol{\lambda}_j^i(\mathbf{r})}, & \text{if } \boldsymbol{\lambda}_j^r(\mathbf{r}) = 0, \\ \frac{1}{\boldsymbol{\lambda}_j^i(\mathbf{r})}\left(\arctan\frac{\boldsymbol{\lambda}_j^r(\mathbf{r})}{\boldsymbol{\lambda}_j^i(\mathbf{r})} + \pi\right), & \text{otherwise.} \end{cases}$$

Let us now consider $\boldsymbol{\lambda}_j^2$ from (13). Here, $|\boldsymbol{f}_j'(t,\mathbf{r})|$ can be described as,

$$|\boldsymbol{f}_j'(t,\mathbf{r})| = \left(\sqrt{\boldsymbol{\lambda}_j^{r2}(\mathbf{r}) + \boldsymbol{\lambda}_j^{i2}(\mathbf{r})}\right) \times e^{\boldsymbol{\lambda}_j^r(\mathbf{r})t}|\cos(\boldsymbol{\lambda}_j^{i2}(\mathbf{r})t - \eta_j(\mathbf{r}))|. \quad (17)$$

While,

$$\eta_j(\mathbf{r}) = \arcsin\left(\frac{\boldsymbol{\lambda}_j^r(\mathbf{r})}{\sqrt{\boldsymbol{\lambda}_j^{r2}(\mathbf{r}) + \boldsymbol{\lambda}_j^{i2}(\mathbf{r})}}\right).$$

Finally, the stationary points of (17) for nonzero $\boldsymbol{\lambda}_j^r(\mathbf{r})$ and $\boldsymbol{\lambda}_j^i(\mathbf{r})$ can be defined as,

$$t_k = \frac{1}{\boldsymbol{\lambda}_j^i(\mathbf{r})}\left(\arctan\frac{\boldsymbol{\lambda}_j^r(\mathbf{r})}{\boldsymbol{\lambda}_j^i(\mathbf{r})} + \frac{\boldsymbol{\lambda}_j^r(\mathbf{r})}{\sqrt{\boldsymbol{\lambda}_j^{r2}(\mathbf{r}) + \boldsymbol{\lambda}_j^{i2}(\mathbf{r})}} + \pi k\right).$$

Note that in (17) the values of $|\cos(\boldsymbol{\lambda}_j^i(\mathbf{r})t_k - \eta_j(\mathbf{r})|$ are the same for every k. Thus, similar to the previous case, the first stationary point corresponds to the value of supremum from (13). With addition of cases with $\boldsymbol{\lambda}_j^r(\mathbf{r}) = 0$ and $\boldsymbol{\lambda}_j^i(\mathbf{r}) = 0$ supremum (13) is reached at:

$$t_j^{**} = \begin{cases} 0, & \text{if } \boldsymbol{\lambda}_j^i(\mathbf{r}) = 0,\\ \frac{\pi - \eta_j(\mathbf{r})}{\boldsymbol{\lambda}_j^i(\mathbf{r})}, & \text{if } \boldsymbol{\lambda}_j^r(\mathbf{r}) = 0,\\ \frac{1}{\boldsymbol{\lambda}_j^i(\mathbf{r})}\arctan\frac{\boldsymbol{\lambda}_j^r(\mathbf{r})}{\boldsymbol{\lambda}_j^i(\mathbf{r})} + \frac{1}{\sqrt{\boldsymbol{\lambda}_j^{r2}(\mathbf{r})+\boldsymbol{\lambda}_j^{i2}(\mathbf{r})}}, & \text{otherwise.}\end{cases}$$

As a result, expression (12) can be written as,

$$\boldsymbol{\mathcal{M}}_i^1(t,\mathbf{r}) = \sum_{j=1}^{m} |\mathbf{h}_{ij}^i(\mathbf{r})| e^{\boldsymbol{\lambda}_j^r(\mathbf{r})t} \mathbf{min}\{|\boldsymbol{\lambda}_j^i(\mathbf{r})|t, 1\}$$
$$+ \sum_{j=1}^{m} |\mathbf{h}_{ij}^r(\mathbf{r})| \mathbf{min}\left\{|\boldsymbol{f}_j(t_j^*, \mathbf{r})|, |\boldsymbol{f}_j'(t_j^{**}, \mathbf{r})|t\right\},$$

Despite the bulky formulation of the bound $\boldsymbol{\mathcal{M}}_i^1(t,\mathbf{r})$, the proposed formulation is just a combination of exponential and piecewise linear functions. Thus, the computational complexity of this function is rather low.

VI. IMPLEMENTATION

Consider Step 4 of Algorithm 1. It solves a computationally tractable optimization problem compared to formulation (3). In this regard, Step 3 formulates a novel frequency assessment $\mathbf{G}(\mathbf{r})$ based on the frequency majorants, as follows,

$$\mathbf{G}(\mathbf{r}) = \max_{i\in\mathbf{N}} \max_{t\in[0,t_{\max}]} \boldsymbol{\mathcal{M}}_i(t,\mathbf{r}). \tag{18}$$

Before approaching the optimization problem (4), it is necessary to calculate inner maximums of (18) within a reasonable time frame. It is noticeable that each $\boldsymbol{\mathcal{M}}_i(t,\mathbf{r})$ is a non-differentiable scalar and uni-modal function. These properties make the golden section [41] one of the best possible choices. The outer maximum is considered over a finite and relatively small set of generators, eliminating the need for any specialized technique. Finally, one can solve (4) using the Quasi-Newton method, as it provides good results for non-smooth optimization [42]. The parameter ϵ was set to as 10^{-2} to make it strictly larger than machine precision, thereby ensuring the stability of the differential system (8).

To showcase the effectiveness of the developed assessment function (18), we will compare it to the direct optimization of frequency nadir $\mathbf{F}(\mathbf{r})$. Similar to (18), nadir is a combination of two maxima. However, unlike in $\mathbf{G}(\mathbf{r})$, the inner maximum is taken over an oscillatory function $|\boldsymbol{\omega}_i(t)|$. As a result, the golden section is inapplicable. The direct optimization (3) utilizes the Branch-and-Bound method with concave overestimators and Differences of Convex Functions (D.C.) approximation [43]. Based on trajectory vector $\boldsymbol{\omega}(t,\mathbf{r})$ derived from the DAE model (5)-(7), it is possible to directly solve the problem (3) by integrating objective (3) along with condition (4b).

To solve the inner maximum of $\mathbf{F}(\mathbf{r})$, we apply D.C. approximation on the oscillatory functions $|\boldsymbol{\omega}_i(t)|$. Let us consider formulation as,

$$\boldsymbol{\omega}_l(t,\mathbf{r}).\boldsymbol{\omega}_i(t,\mathbf{r}) = \mathbf{h}_i(t,\mathbf{r}) - \mathbf{q}_i(t,\mathbf{r}),\ i\in\mathbf{N}. \tag{19}$$

In (19), both $\mathbf{h}_i(t,\mathbf{r})$ and $\mathbf{q}_i(t,\mathbf{r})$ are convex functions in t. Here, $\mathbf{h}_i(t,\mathbf{r}) = \boldsymbol{\omega}_i(t,\mathbf{r}) + \frac{1}{2}\boldsymbol{k}_i(\mathbf{r})t^2$ and $\mathbf{q}_i(t,\mathbf{r}) = \frac{1}{2}\boldsymbol{k}_i(\mathbf{r})t^2$. To calculate $\boldsymbol{k}_i(\mathbf{r})$, we consider second order derivative of $\boldsymbol{\omega}_i(t,\mathbf{r})$ in t. From the (5)-(7), we can obtain this derivative:

$$\frac{\partial^2\boldsymbol{\omega}_i(t,\mathbf{r})}{\partial t^2} = \sum_{j=1}^{m} e^{\Re(\boldsymbol{\lambda}_j(\mathbf{r}))t}\left(\alpha_{ij}(\mathbf{r})\cos(\Im(\boldsymbol{\lambda}_j(\mathbf{r}))t)\right.$$
$$\left.+\beta_{ij}(\mathbf{r})\sin\left(\Im\left(\boldsymbol{\lambda}_j(\mathbf{r})\right)t\right)\right), \tag{20}$$

The variables α_{ij} and β_{ij} from (20) are defined as,

$$\alpha_{ij}(\mathbf{r}) = \Re(\boldsymbol{\lambda}_j(\mathbf{r}))^2\Re(y_{ij}(\mathbf{r}))$$
$$- 2\Re(\boldsymbol{\lambda}_j(\mathbf{r}))\Im(\boldsymbol{\lambda}_j(\mathbf{r}))\Im(y_{ij}(\mathbf{r})) - \Im(\boldsymbol{\lambda}_j(\mathbf{r}))^2\Re(y_{ij}(\mathbf{r})))$$

$$\beta_{ij}(\mathbf{r}) = \Im(\boldsymbol{\lambda}_j(\mathbf{r}))^2\Im(y_{ij}(\mathbf{r}))$$
$$- 2\Re(\boldsymbol{\lambda}_j(\mathbf{r}))\Im(\boldsymbol{\lambda}_j(\mathbf{r}))\Re(y_{ij}(\mathbf{r})) - \Re(\boldsymbol{\lambda}_j(\mathbf{r}))^2\Im y_{ij}(\mathbf{r})).$$

Let us denote $\gamma_{ij}(\mathbf{r}) = \sqrt{\alpha_{ij}^2(\mathbf{r}) + \beta_{ij}^2(\mathbf{r})}$, then, the following lower bound exists for (20),

$$\frac{\partial^2\boldsymbol{\omega}_i(t,\mathbf{r})}{\partial t^2} \geq -\sum_{j=1}^{m}\gamma_{ij}(\mathbf{r})\cos\Big(\Im(\boldsymbol{\lambda}_j(\mathbf{r})t$$
$$+\arcsin\left(\frac{\alpha_{ij}(\mathbf{r})}{\gamma_{ij}(\mathbf{r})}\right)\Big)e^{\Re(\boldsymbol{\lambda}_j(\mathbf{r}))t} \geq -\sum_{j=1}^{m}\gamma_{ij}(\mathbf{r}).$$

Hence, taking $\boldsymbol{k}_i(\mathbf{r}) = \sum_{j=1}^m \gamma_{ij}(\mathbf{r}) \geq 0$ ensures convexity of functions $\mathbf{h}_i(t,\mathbf{r})$ and $\mathbf{q}_i(t,\mathbf{r})$ for all $i\in\mathbf{N}$, as shown in [43]. The D.C. decomposition of $|\boldsymbol{\omega}_i(t,\mathbf{r})|$ has the following representation,

$$|\boldsymbol{\omega}_i(t,\mathbf{r})| = 2\max\{\mathbf{h}_i(t,\mathbf{r}), \mathbf{q}_i(t,\mathbf{r})\} - \mathbf{h}_i(t,\mathbf{r}) - \mathbf{q}_i(t,\mathbf{r}). \tag{21}$$

The inner maximum of (2) incorporates D.C. approximation of the oscillatory functions $|\boldsymbol{\omega}_i(t,\mathbf{r})|$ as (21), and this is solved using a Branch-and-Bound algorithm.

VII. CASE STUDY.

A. Comparison of the Assessment and COI Accuracies

Let us proceed to direct numerical verification of the proposed frequency nadir assessments. Consider four different systems with increasing complexity and size, namely a 3, 10, 16, and 48-machine systems [44]. Results for these systems are summarized in Tables I and II. Information about the maximum frequency deviations, frequency majorants, and COI values are provided in Table I, while Table II displays the corresponding relative errors for both the majorant and COI-based estimates.

TABLE I
FREQUENCY NADIR AND ITS APPROXIMATION

System	Nadir	Maximal $\mathcal{M}$	Maximal $\lvert\mathbf{COI}\rvert$
3 machines	418 (467) mHz	449 (509) mHz	379 (434) mHz
10 machines	330 (337) mHz	395 (459) mHz	226 (258) mHz
16 machines	312 (405) mHz	406 (488) mHz	116 (133) mHz
48 machines	338 (420) mHz	476 (572) mHz	60 (68) mHz

TABLE II
RELATIVE ERRORS OF THE MAJORANTS

System	$\mathcal{M}$ relative error	COI relative error
3 machines	7 (7) %	9 (9) %
10 machines	19 (21) %	31 (32) %
16 machines	30 (20) %	62 (67) %
48 machines	40 (36) %	82 (84) %

TABLE III
RESULTS OF NUMERICAL EXPERIMENTS FOR A 10 MACHINES SYSTEMS

CIG control	Optimization time (s)		Number of calculations		Nadir values (mHz)		
	$\mathbf{F}(\mathbf{r})$	$\mathbf{G}(\mathbf{r})$	$\mathbf{F}(\mathbf{r})$	$\mathbf{G}(\mathbf{r})$	$\mathbf{F}(\mathbf{r}^0)$	$\mathbf{F}(\mathbf{r}^F)$	$\mathbf{F}(\mathbf{r}^G)$
No	10	6	530	565	244	122	102
Yes	22	16	968	1055	244	66	64

Moreover, tests are provided for each system by reducing the inertia of all generators by a factor of $2/3$, showcasing the majorant approach's effectiveness in low-inertia power systems. The results for these low-inertia cases are given in Table I and Table II, respectively (values in brackets are for low-inertia case). Table I clearly demonstrates that in both standard and low inertia cases, the proposed frequency majorant consistently delivers a more conservative estimate of the frequency nadir than the absolute value of COI.

Table II highlights the scalability of the majorant approach. It significantly outperforms COI as the system size increases. For instance, in the case of the small 3-machine system, both methods exhibit relatively similar errors, with the majorant providing a conservative estimate, unlike COI. However, for larger systems with either standard or low inertia, COI shows nearly double the relative errors compared to the derived majorants, even though majorants consistently provide estimates greater than the actual frequency nadir. Consequently, the proposed majorants hold more promising prospects for practical applications.

The next section elaborates on the proposed optimization problem from step 4 of Algorithm 1 and evaluates its performance compared to the approach based on the exact frequency nadir assessment.

B. Comparison With Direct Nadir Optimization

This section provides a detailed performance of the PILOT framework, which was validated using the Power System Toolbox (PST) [6]. As an optimization example, the New England test case was selected. Although we use a simplified model in our theoretical analysis and optimization process, the test case for dynamic performance evaluation utilizes a more detailed power system model. This comprehensive model includes considerations such as line losses and voltage dynamics enabled by PST. As for the synchronous generators, instead of the ideal swing dynamics, 2-axis sub-transient reactance models equipped with multi-stage turbines are adopted in the simulations. Moreover, we explicitly model the dynamics of interfacing converters with the PLL and inner CCL as in [34].

We considered two distinct scenarios for the test case: i) a standard system without any CIGs and ii) a system equipped with 10 CIGs operating alongside traditional generation. In both scenarios, we assumed a partial outage affecting generator 1. Given the overall damping characteristics inherent in the test case, the largest frequency deviations transpire around a 20 seconds time frame. This time frame is critical for evaluating the system's response to the partial outage and its ability to recover from the subsequent frequency deviations. However, it is worth noting that for a weakly connected or less damped grid, the most substantial-frequency oscillations may occur after the initial 20 seconds.

A summary of the numerical assessment is provided in Table III. The column labeled "CIG control" indicates the CIGs' contribution to the primary frequency control. Notably, in both scenarios, whether CIGs participate or not in the optimization algorithm, the assessment $\mathbf{G}(\mathbf{r})$ based on frequency majorants consistently yields better results in terms of computational efficiency and optimal solutions compared to the exact nadir assessment $\mathbf{F}(\mathbf{r})$.

In the case of $\mathbf{F}(\mathbf{r})$, the global maximum of each function $|\boldsymbol{\omega}_i(t,\mathbf{r})|, i \in \mathbf{N}$ is obtained using the Branch and Bound method with concave overestimators and D.C. approximation. Convergence of the algorithmic procedure is described in [43]. For optimization of both $\mathbf{F}(\mathbf{r})$ and $\mathbf{G}(\mathbf{r})$, the vector of the default control parameters $\mathbf{r}^0$ is used in the system as a starting point. The optimal points found by the Quasi-Newton method are denoted by $\mathbf{r}^F$ and $\mathbf{r}^G$ for $\mathbf{F}(\mathbf{r})$ and $\mathbf{G}(\mathbf{r})$, respectively.

The time required for the optimization of $\mathbf{F}(\mathbf{r})$ is higher compared to the optimization of $\mathbf{G}(\mathbf{r})$ as for every calculation of $\mathbf{F}(\mathbf{r})$, the algorithm has to solve "n" number of D.C. optimization problems. On the contrary, for the calculation of $\mathbf{G}(\mathbf{r})$, only golden section computations are performed.

In both scenarios with and without CIG integration, optimization of $\mathbf{G}(\mathbf{r})$ yields a better optimal solution. Fig. 4 illustrate this via contour plots of $\mathbf{F}(\mathbf{r})$ and $\mathbf{G}(\mathbf{r})$. In this representation, all components of the control vector $\mathbf{r}$ are fixed except the first two, which are free to vary, namely r_1 and r_2. Assessment $\mathbf{F}(\mathbf{r})$ is depicted in Fig. 4(a), while Fig. 4(b) outlines $\mathbf{G}(\mathbf{r})$ as functions of these two varying control parameters.

Each curve from Fig. 4(a) and (b) corresponds to a 1-dimensional solution manifold of either $\mathbf{F}(\mathbf{r})$ or $\mathbf{G}(\mathbf{r})$ by varying the value of r_1 while keeping r_2 fixed, and vice versa. Fig. 4 clearly illustrates that function $\mathbf{F}(\mathbf{r})$ contains multiple local optima, such as $\mathbf{F}(\mathbf{r}^F)$ and $\mathbf{F}(\mathbf{r}^G)$, among others. This is due to the fact that $\mathbf{F}(\mathbf{r})$ embodies oscillatory frequency trajectories. In contrast, $\mathbf{G}(\mathbf{r})$ exhibits a distinctive global solution, denoted as $\mathbf{G}(\mathbf{r}^G)$. Since both functions are black boxes, there is no reliable method of avoiding local optima. Therefore, reducing the local minima number, as in the case of $\mathbf{G}(\mathbf{r})$, may result in a better optimization solution.

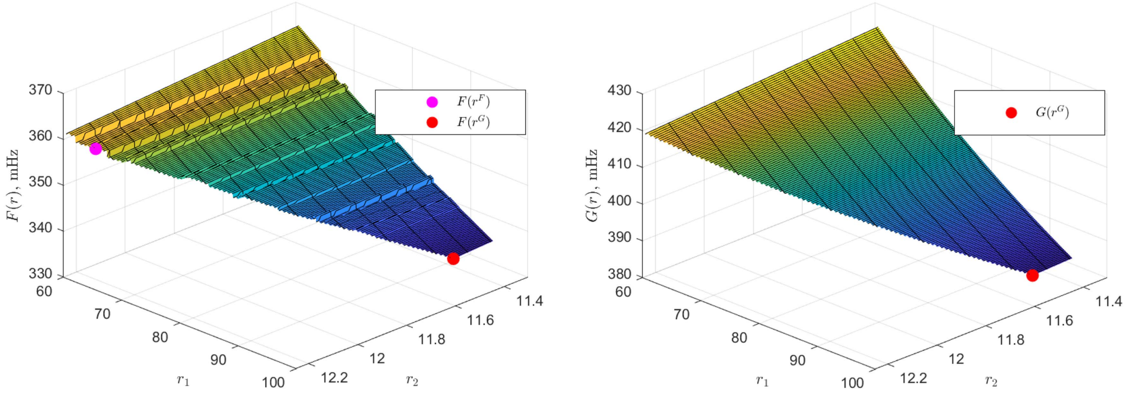

(a)

(b)

Fig. 4. Values of $\mathbf{F}(\mathbf{r})$ and $\mathbf{G}(\mathbf{r})$ for New England system with $\mathbf{r}_i, i = \overline{3,10}$ fixed. Purple and red points denote $\mathbf{r}^F$ and $\mathbf{r}^G$ respectively. (a) Function $\mathbf{F}(\mathbf{r})$. (b) Function $\mathbf{G}(\mathbf{r})$.

TABLE IV
PARAMETERS r BEFORE AND AFTER OPTIMIZATION FOR SYSTEM WITH TRADITIONAL GENERATION ONLY

Gain	**Generator number**									
	1	2	3	4	5	6	7	8	9	10
$\mathbf{r}^0$	20	20	20	20	20	20	20	20	20	20
$\mathbf{r}^F$	267	96	67	58	58	46	46	44	33	30
$\mathbf{r}^G$	60	191	175	139	126	84	76	71	48	35

TABLE V
PARAMETERS $\mathbf{r}$ BEFORE, AFTER OPTIMIZATION AND FOR VIRTUAL INERTIA CONTROL FOR SYSTEM WITH CIG

Gain	**Generator number**									
	1	2	3	4	5	6	7	8	9	10
$\mathbf{r}^0_{\text{SG}}$	20	20	20	20	20	20	20	20	20	20
$\mathbf{r}^0_{\text{CI}}$	0	0	0	0	0	0	0	0	0	0
$\mathbf{r}^F_{\text{SG}}$	207	115	122	91	92	90	90	158	214	94
$\mathbf{r}^F_{\text{CI}}$	40	27	24	24	24	23	23	22	21	21
$\mathbf{r}^G_{\text{SG}}$	131	36	113	13	0	112	140	181	84	258
$\mathbf{r}^G_{\text{CI}}$	0	27	62	54	49	36	33	32	25	23
$\mathbf{r}^{VI}_{\text{SG}}$	20	20	20	20	20	20	20	20	20	20
$\mathbf{r}^{VI}_{\text{CI}}$	20	20	20	20	20	20	20	20	20	20

Let us now review optimal solutions for both scenarios explicitly. Table IV contains control coefficients for the first case, which excludes CIG participation. A clear qualitative difference among optimizing $\mathbf{G}(\mathbf{r})$ and $\mathbf{F}(\mathbf{r})$ is observable. The optimization over $\mathbf{F}(\mathbf{r})$ increases control coefficients proportionally to the electrical distance to the disturbance. In contrast, optimizing $\mathbf{G}(\mathbf{r})$ shows that it is more efficient to maintain coefficient $\mathbf{r}_1$ for stability considerations. While this constraint reduces the response of the first generator, it simultaneously ensures the stability margin required to significantly enhance the control response of neighboring generators, thereby improving overall control quality.

Table V presents control coefficients for the second scenario, where CIGs participate alongside the traditional generation. Here, the vector $\mathbf{r}$ with subscripts "CI" and "SG" denotes the converter interfaced and synchronous generators. In addition to proportional control, this scenario also explores virtual inertia emulation. It considers standard droop control coefficients for both synchronous generators ($\mathbf{r}^{VI}_{\text{SG}}$) and CIGs ($\mathbf{r}^{VI}_{\text{CI}}$). Details of the droop coefficients for the proportional component of CIG control are provided in Table V. The coefficient for the derivative aspect of control, which corresponds to inertia emulation, has been set to 15 seconds. The goal was to take the highest values of virtual inertia that can realistically be implemented [45].

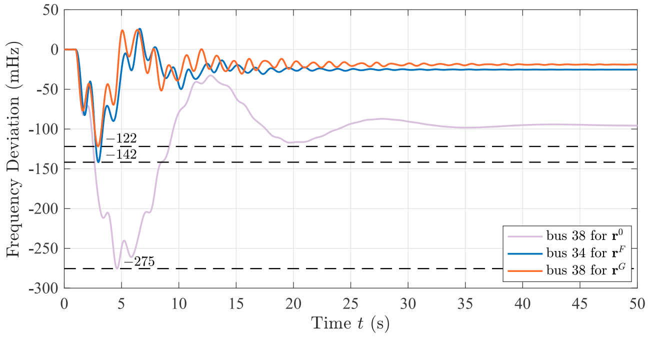

Fig. 5. Frequency deviation for optimized coefficients of generators for system with synchronous generation only.

As observable, the optimization algorithm automatically redistributes the influential control efforts to the CIG and keeps traditional generation almost unchanged. This strategy leverages the rapid dynamics of CIGs to mitigate the initial frequency drop and minimize the deterioration of the conventional generating equipment.

The post-contingency system dynamic responses for both scenarios are shown in Figs. 5 and 6. Each curve from these figures corresponds to the bus with the most substantial frequency oscillations (frequency nadir) under varying control settings, notably bus 38 for $\mathbf{r}^0$, bus 38 for $\mathbf{r}^G$, and bus 34 for $\mathbf{r}^F$. The location where the frequency nadir occurs depends on the control parameters, resulting in distinct curves associated with different bus frequencies. Fig. 5 depicts the system's dynamics when

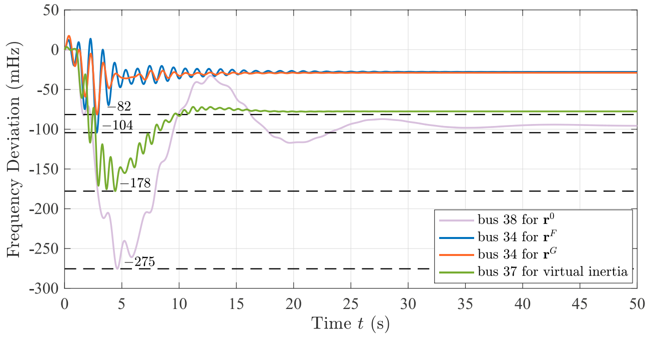

Fig. 6. Frequency deviation for system with CIG.

optimized control gains are applied to synchronous generators exclusively. Whereas Fig. 6 displays the system's behavior when both generation types participate in the proposed frequency response framework. Fig. 6 also outlines an additional trajectory representing frequency for bus 38 when CIG incorporates virtual inertia as part of the control. It is important to emphasize that the pink curve in both figures represents the system's response to the same disturbance when standard droop control gains are applied.

A significant reduction in frequency deviation is evident in both scenarios. However, in the first scenario, where control efforts primarily rely on synchronous generators, the slow turbine dynamics and large control coefficients lead to frequency oscillations and overshoots, as shown in Fig. 5. In the second scenario, redistributing the primary control efforts to the CIGs suppresses these oscillations effectively. It leads the initial deviation convergence to a steady state and follows an almost exponential trajectory, as shown in Fig. 6. Consequently, this demonstrates the effectiveness of the proposed control strategy in enhancing system stability and reducing frequency deviations in the presence of CIGs. Furthermore, it can be observed that the proposed control approach outperforms the virtual inertia approach even though inertia coefficients were set to large values to maximize the effect of emulated inertia.

VIII. CONCLUSION

Large-frequency nadirs pose a significant threat to power system security and reliability. It can potentially lead to load shedding and cascading events. Primary frequency control is deployed to minimize post-contingency frequency deviations, particularly in grids with sufficient inertia. However, as CIG penetration grows, large frequency nadirs are expected due to reduced inertia levels. As a result, traditional frequency control struggles to respond effectively to frequency excursions in low-inertia systems with significant CIG integration.

This work presents a novel "Piece-wise Proportional and Location-sensitive Primary Frequency Control" (PILOT) framework. This framework is tailored to the specific contingency and spatial characteristics, which calculates and distributes proportional controller gains to achieve maximum efficiency of controllable generators without loss of stability. Such a data-driven approach allows a proportional control embedded in control discontinuity, resulting in rapid control actions necessary for the low inertia systems.

The PILOT framework incorporates a novel frequency majorant assessment to overcome the limitations associated with the COI model and exact nadir-based assessments. This approach provides a unimodal conservative estimate of the multi-extremum frequency of each machine, taking into account all system modes. Moreover, it facilitates computationally tractable optimization, reducing the computational complexity and burden compared to exact nadir assessment.

The framework employs an indirect nadir optimization approach for each credible contingency scenario, pre-computing optimal control gains. This allows for real-time operation with minimal demands on information and communication infrastructure. The optimization algorithm comprises entire system dynamics, considering factors such as the electrical distance to the disturbance and the specific type of controlled generation (e.g., converter interfaced, synchronous, or turbine-based). The goal is to optimize frequency control actions for maximum efficiency in addressing various system conditions.

The proposed control algorithm is versatile, accommodating both synchronous and CIGs. It represents an extension of proportional controllers, offering a gradual implementation approach within modern power grids. The numerical results highlight the effectiveness of this primary frequency response in low inertia power systems, encompassing both conventional and CIGs. The control scheme demonstrated a notable 49% reduction in nadir deviation and a 30% reduction in the transient period. Furthermore, the results indicate that optimizing droop control gains based on CIG characteristics, such as their location and dynamics, enables CIGs to effectively assume primary frequency control functions, contributing to the stability of power systems.

REFERENCES

[1] M. A. Hossain, H. R. Pota, M. J. Hossain, and F. Blaabjerg, "Evolution of microgrids with converter-interfaced generations: Challenges and opportunities," *Int. J. Elect. Power Energy Syst.*, vol. 109, pp. 160–186, 2019.

[2] D. Greenwood, K. Y. Lim, C. Patsios, P. Lyons, Y. S. Lim, and P. Taylor, "Frequency response services designed for energy storage," *Appl. Energy*, vol. 203, pp. 115–127, 2017.

[3] A. Fernández-Guillamón, E. Gómez-Lázaro, E. Muljadi, and Á. Molina-García, "Power systems with high renewable energy sources: A review of inertia and frequency control strategies over time," *Renewable Sustain. Energy Rev.*, vol. 115, 2019, Art. no. 109369.

[4] J. Machowski, J. Bialek, and J. Bumby, *Power System Dynamics: Stability and Control*, 2nd ed. Hoboken, NJ, USA: Wiley, 2008.

[5] L. Ferris and D. Infield, *Renewable Energy in Power Systems*, 1st ed. Hoboken, NJ, USA: Wiley, 2008.

[6] P. W. Sauer, M. A. Pai, and J. H. Chow, *Power System Dynamics and Stability: With Synchrophasor Measurement and Power System Toolbox 2e: With Synchrophasor Measurement and Power System Toolbox*, 2nd ed. Hoboken, NJ, USA: Wiley, 2017.

[7] L. Meng et al., "Fast frequency response from energy storage systems–a review of grid standards, projects and technical issues," *IEEE Trans. Smart Grid*, vol. 11, no. 2, pp. 1566–1581, Mar. 2020.

[8] J. Bialek, "What does the GB power outage on 9 Aug. 2019 tell us about the current state of decarbonised power systems?," *Energy Policy*, vol. 146, 2020, Art. no. 111821.

[9] Z. A. Obaid, L. M. Cipcigan, L. Abrahim, and M. T. Muhssin, "Frequency control of future power systems: Reviewing and evaluating challenges and new control methods," *IEEE J. Modern Power Syst. Clean Energy*, vol. 7, no. 1, pp. 9–25, Jan. 2019.

[10] M. D. Ilic, “From hierarchical to open access electric power systems,” *Proc. IEEE*, vol. 95, no. 5, pp. 1060–1084, May 2007.

[11] Z. Wang, F. Liu, S. H. Low, C. Zhao, and S. Mei, “Distributed frequency control with operational constraints, part I: Per-node power balance,” *IEEE Trans. Smart Grid*, vol. 10, no. 1, pp. 40–52, Jan. 2019.

[12] Z. Wang, F. Liu, S. H. Low, C. Zhao, and S. Mei, “Distributed frequency control with operational constraints, part II: Network power balance,” *IEEE Trans. Smart Grid*, vol. 10, no. 1, pp. 40–52, Jan. 2019.

[13] X. Zhang and A. Papachristodoulou, “Distributed dynamic feedback control for smart power networks with tree topology,” in *Proc. Amer. Control Conf.*, 2014, pp. 1156–1161.

[14] X. Zhang and A. Papachristodoulou, “A real-time control framework for smart power networks with star topology,” in *Proc. Amer. Control Conf.*, 2013, pp. 5062–5067.

[15] M. Andreasson, D. V. Dimarogonas, H. Sandberg, and K. H. Johansson, “Distributed control of networked dynamical systems: Static feedback, integral action and consensus,” *IEEE Trans. Autom. Control*, vol. 59, no. 7, pp. 1750–1764, Jul. 2014.

[16] M. Andreasson, D. V. Dimarogonas, H. Sandberg, and K. H. Johansson, “Distributed pi-control with applications to power systems frequency control,” in *Proc. Amer. Control Conf.*, 2014, pp. 3183–3188.

[17] D. Apostolopoulou, P. W. Sauer, and A. D. Domínguez-García, “Balancing authority area model and its application to the design of adaptive AGC systems,” *IEEE Trans. Power Syst.*, vol. 31, no. 5, pp. 3756–3764, Sep. 2016.

[18] M. D. Ilić and J. Zaborsky, *Dynamics and Control of Large Electric Power Systems*. Hoboken, NJ, USA: Wiley, 2000.

[19] M. D. Ilić and S. X. Liu, *Hierarchical Power Systems Control: Its Value in a Changing Electric Power Industry*. New-York: Berlin, Germany: Springer, 1996.

[20] Q. Liu and M. D. Ilić, “Enhanced automatic generation control (E-AGC) for future electric energy systems,” in *Proc. IEEE Power Energy Soc. Gen. Meeting*, 2012, pp. 1–8.

[21] M. F. M. Arani and E. F. El-Saadany, “Implementing virtual inertia in DFIG-based wind power generation,” *IEEE Trans. Power Syst.*, vol. 28, no. 2, pp. 1373–1384, May 2013.

[22] J. Ma, Y. Gu, Y. Shen, Y. Zhou, A. G. Phadke, and P. Cheng, “Stability analysis of power grid connected with direct-drive wind farm containing virtual inertia based on integrated dissipation energy model,” *IEEE Trans. Sustain. Energy*, vol. 12, no. 4, pp. 2378–2392, Oct. 2021.

[23] A. Ashouri-Zadeh and M. Toulabi, “Adaptive virtual inertia controller for DFIGs considering nonlinear aerodynamic efficiency,” *IEEE Trans. Sustain. Energy*, vol. 12, no. 2, pp. 1060–1067, Apr. 2021.

[24] J. Chang, Y. Du, E. G. Lim, H. Wen, X. Li, and L. Jiang, “Coordinated frequency regulation using solar forecasting based virtual inertia control for islanded microgrids,” *IEEE Trans. Sustain. Energy*, vol. 12, no. 4, pp. 2393–2403, Oct. 2021.

[25] P. R. Almeida, F. J. Soares, and J. P. Lopes, “Electric vehicles contribution for frequency control with inertial emulation,” *Electric Power Syst. Res.*, vol. 127, pp. 141–150, 2015.

[26] S. S. Guggilam, C. Zhao, E. Dall’Anese, Y. C. Chen, and S. V. Dhople, “Optimizing DER participation in inertial and primary-frequency response,” *IEEE Trans. Power Syst.*, vol. 33, no. 5, pp. 5194–5205, Sep. 2018.

[27] O. Stanojev, U. Markovic, P. Aristidou, G. Hug, D. Callaway, and E. Vrettos, “MPC-based fast frequency control of voltage source converters in low-inertia power systems,” *IEEE Trans. Power Syst.*, vol. 37, no. 4, pp. 3209–3220, Jul. 2022.

[28] R. K. Subroto, K. L. Lian, C.-C. Chu, and C.-J. Liao, “A fast frequency control based on model predictive control taking into account of optimal allocation of power from the energy storage system,” *IEEE Trans. Power Del.*, vol. 36, no. 4, pp. 2467–2478, Aug. 2021.

[29] U. Markovic, Z. Chu, P. Aristidou, and G. Hug, “LQR-based adaptive virtual synchronous machine for power systems with high inverter penetration,” *IEEE Trans. Sustain. Energy*, vol. 10, no. 3, pp. 1501–1512, Jul. 2019.

[30] O. Stanojev, O. Kundacina, U. Markovic, E. Vrettos, P. Aristidou, and G. Hug, “A reinforcement learning approach for fast frequency control in low-inertia power systems,” in *Proc. IEEE 52nd North Amer. Power Symp.*, 2021, pp. 1–6.

[31] W. Cui, Y. Jiang, and B. Zhang, “Reinforcement learning for optimal primary frequency control: A Lyapunov approach,” *IEEE Trans. Power Syst.*, vol. 38, no. 2, pp. 1676–1688, Mar. 2023.

[32] T. Thacker and H. Pulgar-Painemal, “Improved primary frequency response through deep reinforcement learning,” in *Proc. IEEE North Amer. Power Symp.*, 2022, pp. 1–6.

[33] Y. Zhang, X. Shi, H. Zhang, Y. Cao, and V. Terzija, “Review on deep learning applications in frequency analysis and control of modern power system,” *Int. J. Elect. Power Energy Syst.*, vol. 136, 2022, Art. no. 107744.

[34] Y. Jiang, E. Cohn, P. Vorobev, and E. Mallada, “Storage-based frequency shaping control,” *IEEE Trans. Power Syst.*, vol. 36, no. 6, pp. 5006–5019, Nov. 2021.

[35] North American Electric Reliability Corporation, “Frequency response standard, background document,” 2012. [Online]. Available: https://scholar.google.com/scholar?hl=en&as_sdt=0,10&q=frequency+response+standard,+background+document

[36] N. Miller, M. Shao, S. Pajic, and R. D’Aquila, “Eastern frequency response study,” *Nat. Renewable Energy Lab.*, Golden, CO, USA, Tech. Rep. NREL/SR-5500-58077 AFT-1-11306-1, 2013.

[37] O. O. Khamsiov and V. Terzija, “Distributed frequency control and congestion management with coupling inter-area constraints,” in *Proc. IEEE Belgrade PowerTech*, 2023, pp. 1–6.

[38] J. Zhao et al., “Power system dynamic state estimation: Motivations, definitions, methodologies, and future work,” *IEEE Trans. Power Syst.*, vol. 34, no. 4, pp. 3188–3198, Jul. 2019.

[39] C. Zhao, E. Mallada, S. Low, and J. Bialek, “A unified framework for frequency control and congestion management,” in *Proc. Power Syst. Computation Conf.*, 2016, pp. 1–7.

[40] F. Dorfler and F. Bullo, “Kron reduction of graphs with applications to electrical networks,” *IEEE Trans. Circuits Syst. I: Regular Papers*, vol. 60, no. 1, pp. 150–163, Jan. 2013.

[41] M. S. Bazaraa, H. D. Sherali, and C. M. Shetty, *Nonlinear Programming: Theory and Algorithms*, 3rd ed. Hoboken, NJ, USA: Wiley, 2006.

[42] A. S. Lewis and M. L. Overton, “Nonsmooth optimization via quasi-Newton methods,” *Math. Program.*, vol. 141, no. 1, pp. 135–163, 2013.

[43] R. Horst and H. Tuy, *Global Optimization Deterministic Approaches*, 3rd ed. Berlin, Germany: Springer, 1996.

[44] W. Sauer Peter, M. A. Pai, and H. Chow Joe, *Power System Toolbox*, Hoboken, NJ, USA: Wiley, 2017.

[45] R. Teodorescu, M. Liserre, and P. Rodrigez, *Grid Converters for Photovoltaic and Wind Power Systems*. Hoboken, NJ, USA: Wiley, 2007.

Oleg Olegovich Khamisov received the M.Sc. degree in applied mathematics from Irkutsk State University, Irkutsk, Russia, in 2015, and the Ph.D. degree in engineering systems from the Skolkovo Institute of Science and Technology (Skoltech), Russia in 2020. He is currently an Assistant Professor with Skoltech. His research focuses on development of control algorithms for low-inertia systems.

Mazhar Ali (Graduate Student Member, IEEE) received the M.Sc. degree in energy systems and Ph.D. degree in engineering systems from the Skolkovo Institute of Science and Technology (Skoltech), Moscow, Russia, in 2015 and 2019, respectively, and the additional M.Sc. degree in research and innovation from the Skoltech-Massachusetts Institute of Technology (Skoltech-MIT) Initiative, Boston, MA, USA, 2015. He was also a Visiting Student with the Department of Mechanical Engineering, Massachusetts Institute of Technology, Boston, Cambridge, MA, USA, from 2013 to 2014 and in 2016. He is currently a Postdoctoral Research Associate with the Department of Electrical and Computer Engineering (ECE), University of Central Florida, Orlando, FL, USA. His research interests include developing innovative computational methods to address various technological challenges in power systems, including power systems security assessment, steady-state voltage stability, power-flow solution space, renewable energy integration, and secure and resilient operations of Cyber-Physical Systems.

Timur Sayfutdinov (Member, IEEE) received the Ph.D. degree in engineering systems from the Skolkovo Institute of Science and Technology (Skoltech), Moscow, Russia, in 2020. He worked for two years as a Research Associate with Newcastle University, Newcastle upon Tyne, U.K. Since 2022, he has been with Xi'an Jiaotong-Liverpool University (XJTLU), Suzhou, China, PRC as Assistant Professor. In 2021, he was recognized with the Outstanding Reviewer Award from IEEE Transactions on Power Systems. His research interests include the sustainable development of low-carbon energy systems, including market-based mechanisms for distribution system management, coordinated procurement of distributed flexibility, and application of active network technologies. He is an Associate Editor for e-Prime—*Advances in Electrical Engineering, Electronics and Energy*.

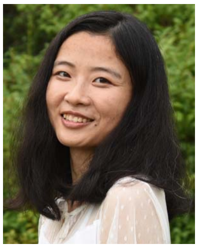

Yan Jiang received the B.Eng. degree in electrical engineering and automation from the Harbin Institute of Technology, Harbin, China, in 2013, the M.S. degree in electrical engineering from the Huazhong University of Science and Technology, Wuhan, China, in 2016, and the Ph.D. degree in electrical engineering with the M.S.E. degree in applied mathematics and statistics from Johns Hopkins University, Baltimore, MD, USA, in 2021. She is currently a Postdoctoral Scholar with the Department of Electrical and Computer Engineering, University of Washington, Seattle, WA, USA. Her research focuses on control of power systems.

Vladimir Terzija was born in Donji Baraci (former Yugoslavia). He received the Dipl-Ing., M.Sc., and Ph.D. degrees in electrical engineering from the University of Belgrade, Belgrade, Serbia, in 1988, 1993, and 1997, respectively. He is currently a Professor of energy systems and networks with the Newcastle University, Newcastle upon Tyne, U.K. He is also a Distinguished Visiting Professor with Shandong University, Jinan, China, and a Guest Professor with the Technical University of Munich, Munich, Germany. During 2021–2023, he was a Full Professor with Skoltech, Russian Federation. During 2006–2020, he was the EPSRC Chair Professor with The University of Manchester, Manchester, U.K. From 2000 to 2006, he was a Senior Specialist for switchgear and distribution automation with ABB, Ratingen, Germany. From 1997 to 1999, he was an Associate Professor with the University of Belgrade, Belgrade, Serbia. His current research interests include smart grid applications, wide-area monitoring, protection and control, multi-energy systems, transient processes, ICT, data analytics, and complex science applications in power systems. He is the Editor-in-Chief of *International Journal of Electrical Power and Energy Systems*, Humboldt Fellow and the recipient of the National Friendship Award, China.

Petr Vorobev received the Ph.D. degree in theoretical physics from the Landau Institute for Theoretical Physics, Moscow, Russia, in 2010. From 2015 to 2018, he was a Postdoctoral Associate with the Department of Mechanical Engineering, Massachusetts Institute of Technology, Cambridge, MA, USA. Since 2019, he has been an Assistant Professor with the Skolkovo Institute of Science and Technology, Moscow, Russia. He joined Nanyang Technological University, Singapore, as a Senior Research Fellow. His research interests include power system dynamics and control, low-frequency oscillations in power systems, dynamics of power system components, multi-timescale approaches to power system modeling, development of plug-and-play control architectures for microgrids.